Biomedicine International (2010) 1: 50-61

Biomedicine International

ORIGINAL ARTICLE

Finite Element Modeling for Solving Pulsatile Flow in a Fusiform Abdominal Aortic Aneurysm

Vijayajothi Paramasivam,[1,4*] Nenad Filipovic,[2, 3] Kanesan Muthusamy,[1] Mohammed Rafiq Abdul Kadir[4]

[1]*Faculty of Science & Technology, Open University Malaysia, Malaysia*
[2]*Faculty of Mechanical Engineering, University of Kragujevac, Kragujevac, Serbia*
[3]*Harvard School of Public Health, Boston, USA*
[4]*Medical Implant Technology Group (MEDITEG), Faculty of Biomedical Engineering & Health Science, Universiti Teknologi Malaysia, Malaysia*

ABSTRACT

Computational modeling is a fundamentally new approach to medical treatment planning and the development of predictive methods for clinical applications. Abdominal aortic aneurysm (AAA) is a common clinical problem that requires determination of hemodynamic conditions and prediction of subsequent rupture. The objective of this paper is to solve a set of three-dimensional nonlinear finite element equations in order to model clinically relevant hemodynamic conditions that are important in predicting the risk of rupture of AAAs. The solution exploits the mixed velocity-pressure (v-p) finite element method by implementing the Galerkin method and the implicit incremental-iterative procedure. The physiologically realistic pulsatile blood flow dynamics imposed upon the AAA model was solved using the Navier-Stokes and continuity equations that represent a viscous incompressible fluid. This pulsatile condition simulates an *in vivo* aorta at rest. The finite element technique developed here was validated using the well-known analytical solution of the Womersley model. The velocity flow fields, flow-induced wall shear stress and pressure distributions from the resulting technique were quantified. *Biomed. Int. 2010; 1: 50-61 ©2010 Biomedicine International, Inc.*

Key Words: Three-dimensional finite element method; Pulsatile flow; Fusiform abdominal aortic aneurysm; Hemodynamics

INTRODUCTION

An aneurysm is an abnormal berry-like or gradual dilatation of any vessel, usually at or near a branch, caused by localized injury or weakness to the vessel wall. A consensus definition of an aneurysm was given in 1991 by the Society of Vascular Surgery and the International Society for Cardiovascular Surgery: a permanent localized dilatation of an artery having at least 50% increase in diameter compared with the expected normal diameter of the artery, or of the diameter of the segment proximal to the dilatation. In general, this indicates that an aorta with a diameter of 3 cm or more is defined as aneurismal, since the maximal diameter of a normal human aorta is about 2 cm.

Abdominal aortic aneurysm (AAA) is a dilatation of the infrarenal abdominal aorta, which lies between the renal bifurcation and the iliac branches. The main causes of aneurysm are arteriosclerosis and cystic medial degeneration, but genetic disorders, aortic malfunction (biomechanical), mycotic infections or arthritis can also be causes. [1]

Another recognized cause of aneurismal disorders is loss of vessel distensibility or increased stiffness of the vessel wall, due to a decrease of wall elastin and increase in collagen content. This loss of distensibility is a general result of aging.

AAA has been found to affect 8.8% of the population over the age of 65 and if left untreated it may lead to rupture.[2] The size of the aneurysm and its rate of expansion are widely associated with the risk of rupture.[3] The decision for surgical intervention in AAA patients is complicated because of the lack of a sufficiently accurate rupture risk index. Based on the results from a number of clinical studies, the maximum/peak transverse diameter (PTD) is widely used.[4,5,6,7] In cases where PTD exceeds 5-6 cm, surgical or endovascular treatment is advised.

Detailed experimental measurements of flow fields and flow-induced wall pressures in fusiform AAA models under pulsatile flow conditions have been

[*]Address correspondence to Vijayajothi Paramasivam, Faculty of Science & Technology,
Open University Malaysia, 50480 Kuala Lumpur, Malaysia. E-mail: vjjothi@yahoo.com.

Submitted May 12, 2010; accepted in revised form June 15, 2010.

Advance Access Publication June 25, 2010 (see www.bmijournal.org)

quantified, and the consequent wall shear stresses (WSS) were evaluated from the velocity measurements for various AAA sizes ranging from the smallest to the biggest bulge diameter. It was concluded that as the bulge diameter of the AAA increased, unstable flow occurred.[8] However, "small" (< 5 cm) PTD aneurysms do rupture as well.[9] Therefore, the physiological processes associated with AAA development and progression are not yet fully understood.

Physiological experiments also show that AAA is related to hemodynamic factors.[10] Studies on AAA models were carried out using flow visualization and laser Doppler velocimetry to characterize flow under resting and exercise conditions. Flow was characterized for two AAA model shapes and sizes, simulating early AAA development through moderate growth. It was concluded that AAA flow was divided into three regimes: (i) attached flow over the entire cycle in small AAAs under resting conditions, (ii) vortex formation and translation in moderate size AAAs under resting conditions, and (iii) vortex formation, translation and bursting into turbulence in moderate size AAAs under exercise conditions. [11]

The limited number of experimental measurement techniques reported to date has been compensated by the use of numerical simulations to achieve better understanding of the relationship between cardiovascular diseases and hemodynamic factors. Computational fluid dynamics (CFD) can be a powerful tool for investigating complex structures of blood flow, especially in view of the limitations and difficulties of direct measurements of vascular flow systems. Mathematical models can also help to interpret noninvasive monitoring techniques.

The numerical methods used to study AAA development differ from one researcher to another. However, the finite element method is commonly used nowadays.[12,13,14] The key factor determining the reliability of the finite element scheme is its stability. Generally, the finite element computation of incompressible flows involves two main sources of potential numerical instabilities associated with the Galerkin formulation of the problem. One source is the presence of advection terms in the governing equations, and this can result in spurious node-to-node oscillations primarily in the velocity field. Such oscillations become more apparent for advection-dominated (i.e. high Reynolds number) flows and flows with sharp layers in the solution. The other source of instability is inappropriate combinations of interpolation functions to represent the velocity and pressure fields. These instabilities usually appear as oscillations primarily in the pressure field. In recent decades a number of stabilization procedures have been developed to prevent these potential numerical instabilities.[15,16,17,18,19] In order to guarantee the stability of the scheme, the finite elements for velocity and pressure need to be selected in a way that satisfies the Ladyzhenskaya-Babuska-Brezzi (LBB) condition.[20]

There have been several attempts to use three-dimensional finite element modeling techniques to quantify blood flow dynamics, especially for clinical problems such as AAAs. Numerical tools such as FLOW3D have been used to predict the three-dimensional flow through the rigid wall of the human abdominal aorta, complete with iliac and renal arteries.[21, 22] Also, a finite element method to predict the three-dimensional pulsatile flow in a model of a normal human abdominal aorta under rest and exercise conditions has been used successfully.[23] The anatomical dimensions of the idealized abdominal aorta model were obtained primarily from Moore et al.[24]. The calculated flow patterns coincided with previous experimental results. A recirculation zone was observed to form along the posterior wall of the aorta immediately distal to the renal vessels under resting conditions. Low time-averaged wall shear stress was present in this location, along the posterior wall opposite the superior mesenteric artery and along the anterior wall between the superior and inferior mesenteric arteries. Shear stress temporal oscillations, as measured with an oscillatory shear index (OSI), were elevated in these regions.

The aim of this work is to solve three-dimensional nonlinear finite element equations in order to model clinically relevant hemodynamic conditions that are important for predicting the risk of rupture of AAAs. The solution exploits the mixed velocity-pressure (v-p) finite element method by implementing the Galerkin method and the implicit incremental-iterative procedure. The results from this method are validated by comparing the hemodynamic conditions reported in a typical AAA established experimentally.

METHODS AND MATERIALS

Fusiform AAA geometry

An idealized fusiform-shaped AAA in the straight aorta domain was analyzed; aorta proximal and distal to the AAA bulge was considered a straight, sufficiently long rigid tube, thus ensuring that a fully developed flow field entered the model bulge. Branching arteries were excluded. The AAA model had a straight non-dilated aorta diameter, $d_{AA} = 18$ mm, length of AAA, $L_{AAA} = 4d_{AA}$ and a diameter ratio, i.e. $\frac{d_{AAA}}{d_{AA}} = 2.75$, where d_{AAA} is the maximum diameter of the AAA bulge, as shown in Figure 1.[8]

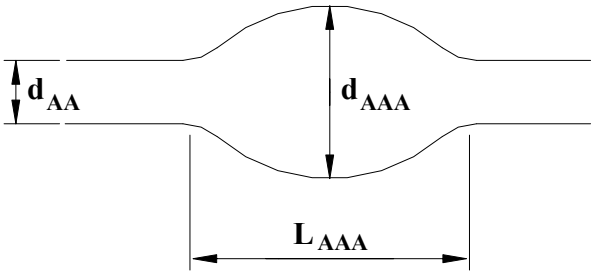

Figure 1. Fusiform AAA geometry

Governing equations for incompressible viscous fluid flow

Except in very tiny capillaries, blood flow can be assumed to behave as a continuum, as well as being incompressible.[25] The three-dimensional equations (momentum and continuity equations) governing the flow of a viscous incompressible Newtonian fluid (blood), using the indicial notations with the usual summation convention, are respectively:-

$$\rho\left(\frac{\partial v_i}{\partial t}+v_j v_{i,j}\right)=\sigma_{ij,j}+f_i^B \qquad (1)$$

$$v_{i,i}=0 \qquad (2)$$

where v_i is the velocity of blood flow in direction x_i, and summation is assumed on the repeated (dummy) indices i, j = 1, 2, 3. ρ, $\sigma_{ij,j}$ and f_i^B are the fluid density, fluid stress and body force, respectively. The prescribed velocity on the surface S_1 and boundary force on the surface S_2 as the governing boundary conditions imposed on Equations (1) and (2) are, respectively:-

$$v_i=\bar{v}_i\big|_{S_1} \qquad (3)$$

$$\sigma_{ij}n_j=f_i^S\big|_{S_2} \qquad (4)$$

where the fluid domain of interest S with its boundaries is given as:-

$$S_2\cup S_1=S \text{ and } S_2\cap S_1=\varnothing \qquad (5)$$

Next, a constitutive equation for the fluid stress for a Newtonian fluid is introduced as:-

$$\sigma_{ij}=-p\delta_{ij}+2\mu\dot{e}_{ij} \qquad (6)$$

where p is the fluid pressure, μ is the dynamic viscosity of the fluid, $\dot{e}_{ij}$ is the tensor of velocity deformation, $\dot{e}_{ij}=\frac{1}{2}\left(\frac{\partial v_i}{\partial x_j}+\frac{\partial v_j}{\partial x_i}\right)$ and δ_{ij} is the Kronecker delta. Substituting Equation (6) into Equation (1) and subsequently applying Equation (2) yields the final form of the flow equation:-

$$\rho\left(\frac{\partial v_i}{\partial t}+v_j v_{i,j}\right)=-p_{,i}+\mu v_{i,jj}+f_i^B \qquad (7)$$

Pulsatile flow and boundary conditions

A physiologically realistic pulsatile blood flow simulating an *in vivo* cardiac cycle of the abdominal aorta section at rest was imposed at the inlet of the non-dilated aorta entry, as shown in Figure 2. The mean Reynolds number, $\mathrm{Re}_{mean}=\frac{4Q_{mean}}{\pi\nu d_{AA}}$, and peak Reynolds Number, $\mathrm{Re}_{peak}=\frac{4Q_{peak}}{\pi\nu d_{AA}}$, of the pulsatile flow were 525 and 2325, respectively. The mean Reynolds number is based on the mean flow rate, Q_{mean}, of a full cardiac cycle, whereas the peak Reynolds number is based on the peak systolic flow rate, Q_{peak}, of the pulsatile flow. The pulsatile flow consists of a pulse frequency, ω, of 60 beats/min, so that the Womersley number $\alpha=\frac{d_{AA}}{2}\sqrt{\frac{\omega}{\nu}}\approx 12$, where ν is the kinematic viscosity of blood, which was taken to be 3.5 $mm^2\ s^{-1}$.

At the inlet of the aorta, the pulsatile flow imposed is considered to be a fully developed flow in an infinitely long straight cylindrical tube. All velocity components at the fixed vessel wall of the AAA model are prescribed as zero. The no-slip condition at the inner vessel wall was adopted. Along the symmetric plane of the model, the velocity components normal to this plane and the tangential stresses are also considered to be zero. At the outlet of the aorta, the normal and tangential stresses are also set at zero (i.e. stress-free condition). Therefore, the solution near the outlet of the aorta differs from the solution in an infinitely long straight cylindrical tube model.

Finite Element Procedure

The mixed velocity-pressure (v-p) finite element formulation was used to solve the nonlinear Navier-Stokes equations. The advantage of this formulation is that the pressure, velocity, velocity gradient and stress boundary conditions can be directly incorporated into the finite element matrix equations.[20] A 21/8 node 3D brick element was used for this three-dimensional

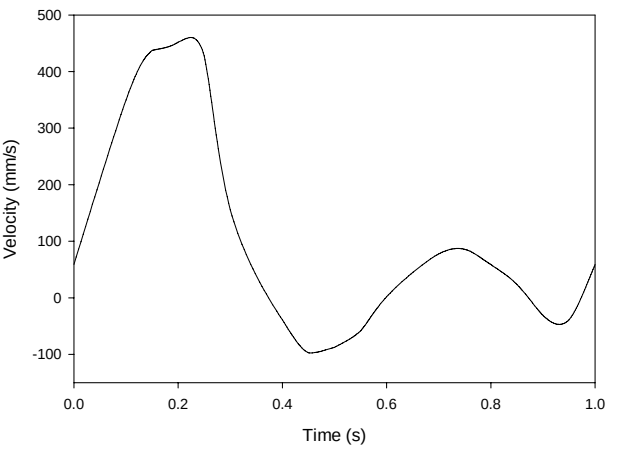

Figure 2. Pulsatile waveform imposed at the entry of the aorta

analysis. Twenty-one nodes were employed to interpolate the velocities and eight nodes were employed to interpolate the pressure, hence providing the stable elements expressed by the inf-sup condition of Brezzi-Babuska. The finite element mesh of the model consists of 7,200 elements and 8,450 nodes.

Applying the Galerkin method to Equations (2) and (7) yields:-

$$\int_V G_\delta v_{i,i} dV = 0 \tag{8}$$

$$\rho\int_V H_\alpha \frac{\partial v_i}{\partial t} dV + \rho\int_V H_\alpha v_j v_{i,j} dV = -\int_V H_\alpha p_{,i} dV + \int_V \mu H_\alpha v_{i,jj} dV + \int_V H_\alpha f_i^B dV \tag{9}$$

Integrating by parts and transforming the volume to surface integral of Equation (9) yields:-

$$\rho\int_V H_\alpha \frac{\partial v_i}{\partial t} dV + \rho\int_V H_\alpha v_j v_{i,j} dV - \int_V H_{\alpha,i} p dV + \int_V \mu H_{\alpha,j} v_{i,j} dV = \int_V H_\alpha f_i^B dV + \int_S H_\alpha \left(-pn_i + \mu v_{i,j} n_j\right) dS \tag{10}$$

The chosen interpolation functions for the velocity and pressure are, respectively:-

$$v_i = H_\alpha v_{i\alpha} \tag{11}$$

$$p = G_\delta p_\delta \tag{12}$$

Next, Equations (11) and (12) are substituted into Equations (10) and (8) to arrive at:-

$$\left[\rho\int_V H_\alpha H_\beta dV\right]\dot{v}_{\beta i} + \left[\rho\int_V H_\alpha H_\gamma v_{j\gamma} H_{\beta,j} dV\right] v_{\beta i} + \left[\int_V \mu H_{\alpha,j} H_{\beta,j} dV\right] v_{\beta i} - \left[\int_V H_{\alpha,i} G_\beta dV\right] p_\beta = \int_V H_\alpha f_i^B dV + \int_S H_\alpha \left(-pn_i + v_{i,j} n_j\right) dS \tag{13}$$

$$\left[\int_V G_\delta H_{\alpha,i} dV\right] v_{\alpha i} = 0 \tag{14}$$

Finally, the finite element matrix equation takes the form:-

$$\begin{bmatrix} \mathbf{M_v} & \mathbf{0} \\ \mathbf{0} & \mathbf{0} \end{bmatrix} \begin{Bmatrix} \dot{\mathbf{v}} \\ \dot{\mathbf{p}} \end{Bmatrix} + \begin{bmatrix} \mathbf{K_{vv}} + \mathbf{K}_{\mu\nu} & \mathbf{K_{vp}} \\ \mathbf{K_{vp}^T} & \mathbf{0} \end{bmatrix} \begin{Bmatrix} \mathbf{v} \\ \mathbf{p} \end{Bmatrix} = \begin{Bmatrix} \mathbf{R_B} + \mathbf{R_S} \\ \mathbf{0} \end{Bmatrix} \tag{15}$$

where the mass, convective, viscosity, pressure gradient, volume force and surface force terms are, respectively:-

$$\left(\mathbf{M_v}\right)_{i\alpha\beta} = \rho\int_V H_\alpha H_\beta dV = \rho\int_V \mathbf{H}^T \mathbf{H} dV$$

$$\left(\mathbf{K_{VV}}\right)_{i\alpha\beta} = \rho\int_V H_\alpha H_\gamma v_{j\gamma} H_{\beta,j} dV = \rho\int_V \mathbf{H^T}\left(\mathbf{H}v_1\mathbf{H}_{,x_1} + \mathbf{H}v_2\mathbf{H}_{,x_2} + \mathbf{H}v_3\mathbf{H}_{,x_3}\right) dV$$

$$\left(\mathbf{K}_{\mu\nu}\right)_{i\alpha\beta} = \int_V \mu H_{\alpha,j} H_{\beta,j} dV = \int_V \mu\left(\mathbf{H}_{,x_1}^T\mathbf{H}_{,x_1} + \mathbf{H}_{,x_2}^T\mathbf{H}_{,x_2} + \mathbf{H}_{,x_3}^T\mathbf{H}_{,x_3}\right) dV$$

$$\left(\mathbf{K_{vp}}\right)_{i\alpha\delta} = -\int_V H_{\alpha,i} G_\delta dV = -\int_V \mathbf{H}_{,\mathbf{x}}^T \mathbf{G} dV$$

$$\left(\mathbf{R_B}\right)_{i\alpha} = \int_V H_\alpha f_i^B dV = \int_V \mathbf{H}^T \mathbf{f^B} dV$$

$$\left(\mathbf{R_S}\right)_{i\alpha} = \int_S H_\alpha \left(-pn_i + v_{i,j} n_j\right) dS = \int_S \mathbf{H}^T\left(-p\mathbf{n} + \mathbf{v}_{,\mathbf{x}} \cdot \mathbf{n}\right) dS \tag{16}$$

Next, in order to implement the incremental-iterative procedure, the velocity and pressure at the end of each time step are defined, respectively:-

$${}^{t+\Delta t}v_{i\alpha} = {}^{t+\Delta t}v_{i\alpha}^{(m-1)} + \Delta v_{i\alpha}^{(m)} \tag{17}$$

$${}^{t+\Delta t}p_\delta = {}^{t+\Delta t}p_\delta^{(m-1)} + \Delta p_\delta^{(m)} \tag{18}$$

where *(m)* is iteration. Next, by substituting Equations (17) and (18) into Equations (13) and (14), the incremental-iterative equation becomes:-

$$\left[\rho\frac{1}{\Delta t}\int_V H_\alpha H_\beta dV\right]\left(\Delta v_{\beta i}^{(m)}\right) + \left[\rho\int_V H_\alpha H_\gamma {}^{t+\Delta t}v_{j\gamma}^{(m-1)} H_{\beta,j} dV\right]\left(\Delta v_{\beta i}^{(m)}\right) + \left[\rho\int_V H_\alpha H_{\gamma,j} {}^{t+\Delta t}v_{j i}^{(m-1)} H_\beta dV\right]\left(\Delta v_{\beta i}^{(m)}\right) + \left[\int_V \mu H_{\alpha,j} H_{\beta,j} dV\right]\left(\Delta v_{\beta i}^{(m)}\right) - \left[\int_V H_{\alpha,i} G_\delta dV\right]\left(\Delta p_\delta^{(m)}\right) = \int_V H_\alpha f_i^B dV + \int_S H_\alpha\left(-pn_i + v_{i,j} n_j\right) dS - \left[\rho\frac{1}{\Delta t}\int_V H_\alpha H_\beta dV\right]\left({}^{t+\Delta t}v_{\beta i}^{(m-1)} - {}^{t}v_{\beta i}\right) - \left[\rho\int_V H_\alpha H_\gamma {}^{t+\Delta t}v_{j i}^{(m-1)} H_{\beta,j} dV\right]\left({}^{t+\Delta t}v_{\beta i}^{(m-1)}\right) - \left[\int_V \mu H_{\alpha,j} H_{\beta,j} dV\right]\left({}^{t+\Delta t}v_{\beta i}^{(m-1)}\right) - \left[\int_V H_{\alpha,i} G_\delta dV\right]\left({}^{t+\Delta t}p_\delta^{(m-1)}\right) \tag{19}$$

$$\left[\int_V G_\delta H_{\alpha,i} dV\right]\left(\Delta v_{\alpha i}^{(m)}\right) = -\left[\int_V G_\delta H_{\alpha,i} dV\right]\left({}^{t+\Delta t}v_{\alpha i}^{(m-1)}\right) \tag{20}$$

Now Equation (15) becomes:-

$$\begin{bmatrix} \frac{1}{\Delta t}\mathbf{M}_{\mathbf{v}} + {}^{t+\Delta t}\mathbf{K}_{\mathbf{vv}}^{(m-1)} + {}^{t+\Delta t}\mathbf{K}_{\mu\mathbf{v}}^{(m-1)} + {}^{t+\Delta t}\mathbf{J}_{\mathbf{vv}}^{(m-1)} & \mathbf{K}_{\mathbf{vp}} \\ \mathbf{K}_{\mathbf{vp}}^{\mathbf{T}} & \mathbf{0} \end{bmatrix} \begin{Bmatrix} \Delta\mathbf{v}^{(m)} \\ \Delta\mathbf{p}^{(m)} \end{Bmatrix} = \begin{Bmatrix} {}^{t+\Delta t}\mathbf{F}_{\mathbf{v}}^{(m-1)} \\ {}^{t+\Delta t}\mathbf{F}_{\mathbf{p}}^{(m-1)} \end{Bmatrix} \quad (21)$$

where the matrices and vectors are:-

$$(\mathbf{M}_{\mathbf{v}})_{i\alpha\beta} = \rho\int_V H_\alpha H_\beta dV = \rho\int_V \mathbf{H}^T\mathbf{H}dV$$

$${}^{t+\Delta t}(\mathbf{K}_{\mathbf{vv}})_{i\alpha\beta}^{(m-1)} = \rho\int_V H_\alpha H_\gamma \, {}^{t+\Delta t}v_{j\gamma}^{(m-1)} H_{\beta,j} dV = \rho\int_V \mathbf{H}^{\mathbf{T}}(\mathbf{H}^{t+\Delta t}\mathbf{v}^{(m-1)})\nabla^T\mathbf{H}dV$$

$${}^{t+\Delta t}(\mathbf{K}_{\mu\mathbf{v}})_{i\alpha\beta}^{(m-1)} = \int_V \mu H_{\alpha,j} H_{\beta,j} dV = \int_V \mu\nabla\mathbf{H}^T\nabla^T\mathbf{H}dV$$

$${}^{t+\Delta t}(\mathbf{J}_{\mathbf{vv}})_{j\alpha\beta}^{(m-1)} = \rho\int_V H_\alpha H_{\gamma,j} \, {}^{t+\Delta t}v_{i\gamma}^{(m-1)} H_\beta dV = \rho\int_V \mathbf{H}^{\mathbf{T}}(\nabla\mathbf{H}^{t+\Delta t}\mathbf{v}^{(m-1)})\mathbf{H}dV$$

$$(\mathbf{K}_{\mathbf{vp}})_{i\alpha\delta} = -\int_V H_{\alpha,i} G_\delta dV = -\int_V \nabla\mathbf{H}^T\mathbf{G}dV$$

$${}^{t+\Delta t}\mathbf{F}_{\mathbf{v}}^{(m-1)} = {}^{t+\Delta t}\mathbf{R}_{\mathbf{B}} + {}^{t+\Delta t}\mathbf{R}_{\mathbf{S}}^{(m-1)} - \left({}^{t+\Delta t}\mathbf{K}_{\mathbf{vv}}^{(m-1)} + {}^{t+\Delta t}\mathbf{K}_{\mu\mathbf{v}}^{(m-1)}\right){}^{t+\Delta t}\mathbf{v}^{(m-1)} - \mathbf{K}_{\mathbf{vp}} \, {}^{t+\Delta t}\mathbf{p}^{(m-1)}$$

$${}^{t+\Delta t}\mathbf{F}_{\mathbf{p}}^{(m-1)} = -\mathbf{K}_{\mathbf{vp}}^{T} \, {}^{t+\Delta t}\mathbf{v}^{(m-1)}$$

$${}^{t+\Delta t}(\mathbf{R}_{\mathbf{B}})_{i\alpha} = \int_V H_\alpha \, {}^{t+\Delta t}f_i^{B} dV = \int_V \mathbf{H}^{T} \, {}^{t+\Delta t}\mathbf{f}^{\mathbf{B}} dV$$

$${}^{t+\Delta t}(\mathbf{R}_{\mathbf{S}})_{i\alpha}^{(m-1)} = \int_S H_\alpha\left(-{}^{t+\Delta t}p^{(m-1)}n_i + {}^{t+\Delta t}v^{(m-1)}{}_{i,j}n_j\right)dS = \int_S \mathbf{H}^T\left(-{}^{t+\Delta t}p^{(m-1)}\mathbf{n} + \nabla^{t+\Delta t}\mathbf{v}^{(m-1)}\cdot\mathbf{n}\right)dS \quad (22)$$

The left upper index $t+\Delta t$ denotes that the quantities are evaluated at the end of the time step. V and S are the volume and the surface of the finite element, respectively. The matrices **H** and **G** contain the interpolation functions for the velocities and the pressure, respectively. The matrix $\mathbf{M}_{\mathbf{v}}$ is the mass matrix, $\mathbf{K}_{\mathbf{vv}}$ and $\mathbf{J}_{\mathbf{vv}}$ are convective matrices, $\mathbf{K}_{\boldsymbol{\mu}\mathbf{v}}$ is the viscosity matrix, $\mathbf{K}_{\mathbf{vp}}$ is the pressure matrix and $\mathbf{F}_{\mathbf{v}}$ and $\mathbf{F}_{\mathbf{p}}$ are forcing vectors.

RESULTS & DISCUSSION

In order to assess the accuracy of the finite element method employed, the pulsatile flow in a typical circular artery was computed and compared with the well-known analytical Womersley solution.[26,27] The Womersley solution reflects how pulsatile flow of a Newtonian fluid travels in a rigid, long, straight tube with periodic velocity. An idealized cylindrical artery with length L and radius r is subjected to an inflow velocity that is uniform in space and periodic in time. The time variation is described by a sinusoidal function $V(t) = \vec{V}\left(1+\sin\left(2\pi\frac{t}{T}\right)\right)$, with mean velocity $\vec{V} = 135 \;\; mm \;\; s^{-1}$ and period $T = 0.2\,s$ as shown in Figure 3.

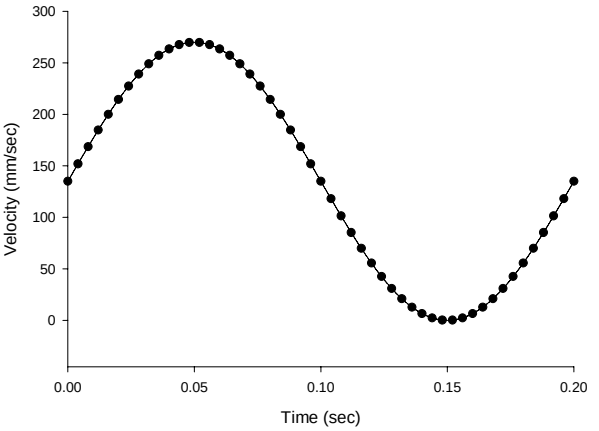

Figure 3. Sinusoidal velocity profile

At a sufficient distance from the inlet, the radial and circumferential components of velocity and pressure vanish. The axial velocity becomes a function of radius only and the pressure varies linearly with axial position. Figures 4 and 5 illustrate the numerically computed axial velocities and the velocity profiles at four different phases within one cardiac cycle for flow in a long, straight, cylindrical tube: t/T = 0.125, t/T = 0.375, t/T = 0.625 and t/T = 0.875. In each of these figures and thereafter, the blood flow direction is indicated by the arrow and the various phases of the pulsatile flow

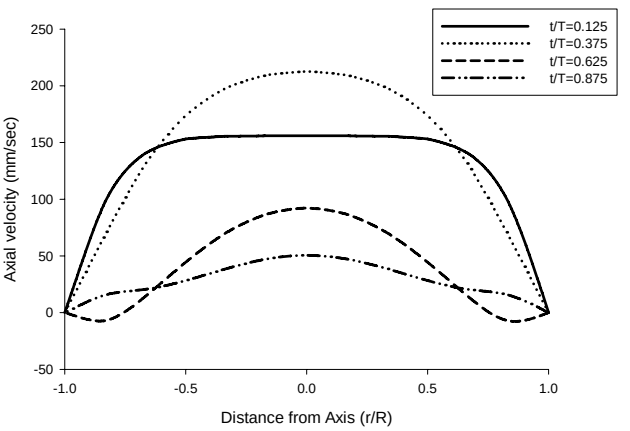

Figure 4. Numerically computed axial velocity at four different phases within one cardiac cycle

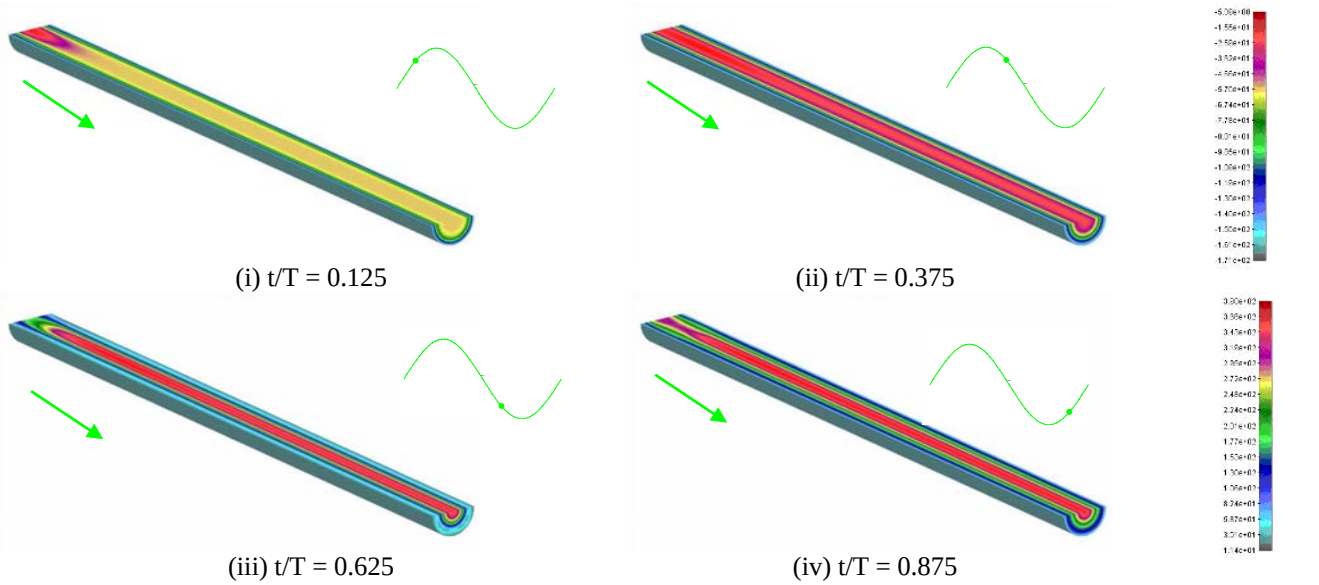

Figure 5. 3D Velocity profiles at four different phases within one cardiac cycle: (i) t/T=0.125; (ii) t/T= 0.375; (iii) t/T = 0.625; (iv) t/T=0.875.

are indicated by the flow waveform icon.

Figures 6 and 7 illustrate the three-dimensional and two-dimensional velocity flow field contours and vectors within the fusiform AAA model, respectively, at six different phases of the pulsatile flow: (i) acceleration to systole, t/T=0.035; (ii) peak systole, t/T=0.16; (iii) deceleration into retrograde flow, t/T=0.35; (iv) peak retrograde flow, t/T=0.55; (v) early diastole, t/T=0.77; and (vi) late diastole, t/T=0.87. Figure 8 illustrates the three-dimensional velocity vectors only within the AAA model during the same six phases of pulsatile flow.

Although the velocities were higher at peak systole than during flow acceleration, the flow moved forward

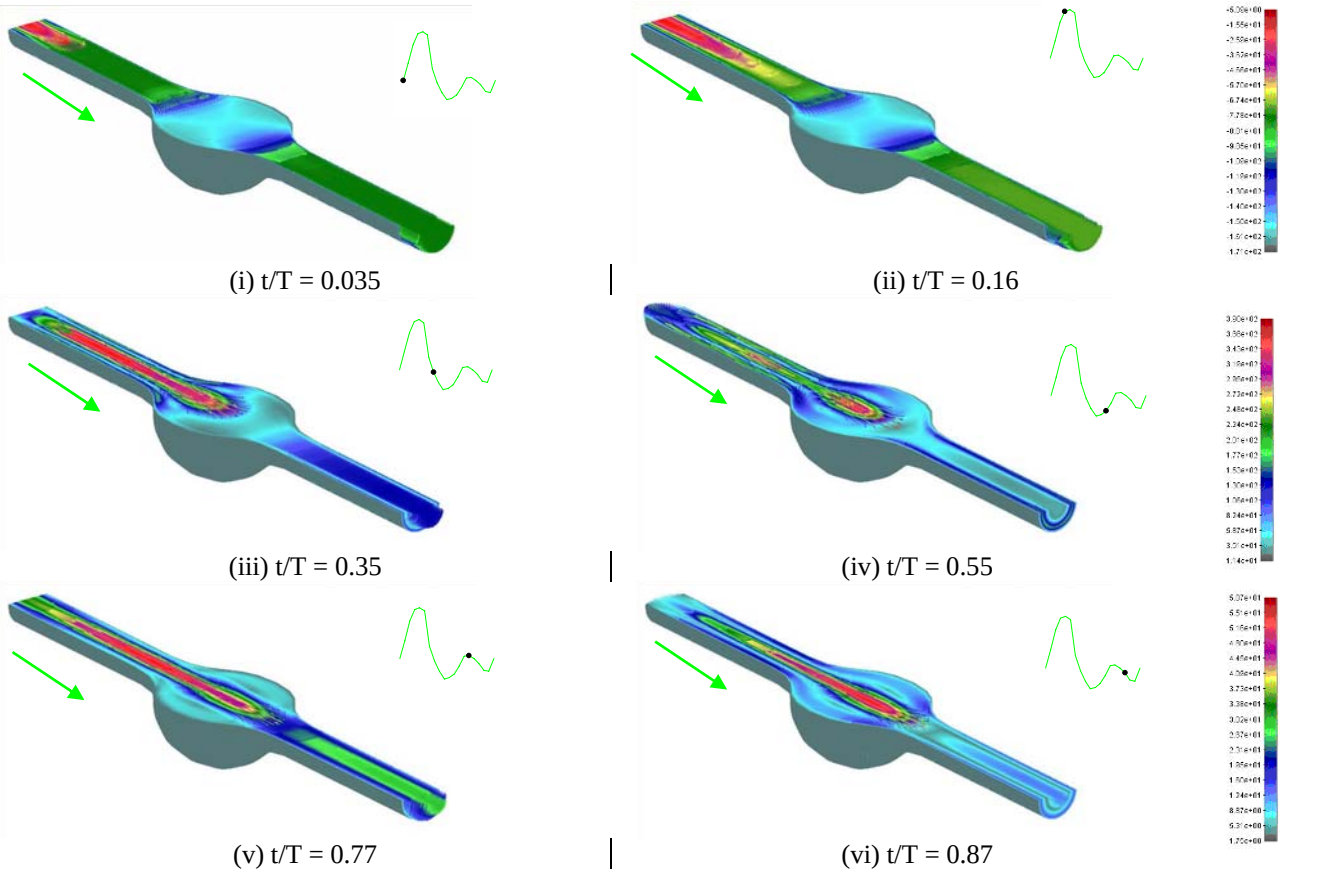

Figure 6. 3D Velocity flow fields at six phases of the pulsatile flow cycle: (i) flow acceleration, t/T=0.035; (ii) peak systole, t/T=0.16; (iii) flow deceleration, t/T=0.35; (iv) peak retrograde flow, t/T=0.55; (v) early diastole, t/T=0.77; (vi) late diastole, t/T=0.87.

uniformly (i.e. attached flow that followed the contour of the wall) throughout the model bulge. There were no vortex formations within the model bulge during acceleration to systole or at peak systole. This is because all the vortices formed at the end of the diastolic phase from the previous pulsatile cycle are pushed out of the aneurysm model and the flow subsequently reattached to the wall as seen in Figures 6 (i), 6 (ii), 7 (i), 7 (ii), 8 (i) and 8 (ii). However, there is a difference in uniformity between the flow entering the proximal zone of the model bulge (i.e. the entrance of the AAA model bulge) and the flow exiting from the distal zone (i.e. the exit of the AAA model bulge). The flow at the exit of the model bulge was more uniform than that at the entrance because as the fluid flowed towards the distal zone of the model bulge, re-constriction at the model exit led to rapid changes in the velocity near the wall.

The deceleration from the peak systolic flow into the retrograde flow region is illustrated in Figures 6 (iii), 7 (iii) and 8 (iii). During this phase of pulsatile flow, a much more rounded velocity profile was observed at the entrance of the model. At the proximal zone of the model bulge, the first appearance of separation or recirculation in the flow cycle was evident. This initial development of a recirculation vortex was caused by the reversed velocities (i.e. in the opposite direction of flow) along the wall at the proximal zone of the model bulge. However, this vortex formation was limited to the proximal half of the model bulge.

At the peak retrograde flow region, the length of the recirculation vortex increased up to the central region of the model bulge, as shown in Figures 6 (iv) and 7 (iv). However, as the peak retrograde flow developed, the fluid flow reversed its direction and the traveled from the distal zone towards the proximal zone along the wall of the model bulge, and also along the non-dilated vessel wall located before the entrance to the bulge, as shown in Figure 8 (iv). This reversed flow eventually converged at the proximal zone of the model bulge along the wall. In contrast, the velocity and the flow in the core region of the model, i.e. along the central symmetric plane, still exhibited forward movement.

As the flow emerged from the retrograde into the early diastolic flow region, the net flow decelerated back to zero. During early diastolic flow, the velocity at the proximal zone of the model bulge was reduced. The velocity at the proximal zone closer to the bulge wall became almost zero.

In contrast to the velocity at the proximal zone of the model bulge, the momentum of the flow at the distal zone was not fully reduced. Although flow in the core region along the central symmetric plane of the model still travelled in the forward direction, an outer region of retrograde motion surrounded it. This contributed to the presence of double recirculation vortices at the distal zone of the model bulge, as shown in Figures 6 (v), 7 (v) and 8 (v). During late diastolic flow, these double recirculation vortices dissipated and a nearly irrotational weak forward-moving flow field was observed

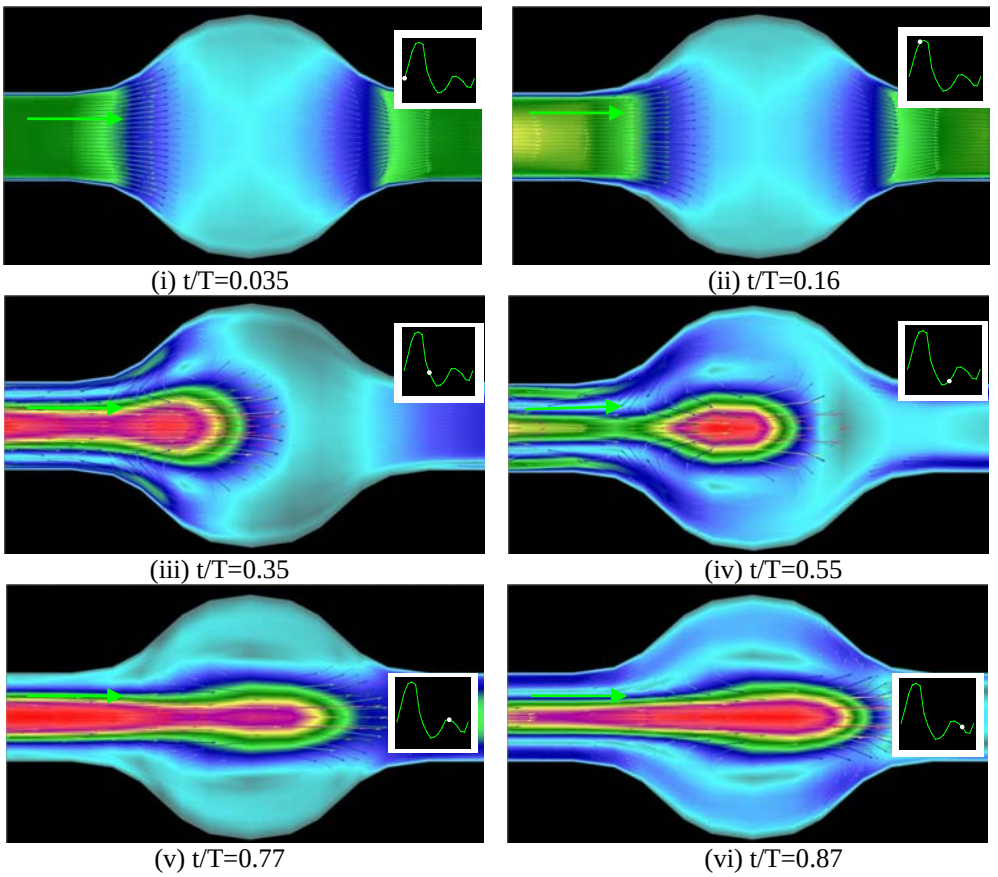

Figure 7. 2D Velocity flow field contours and vectors at six phases of the pulsatile flow cycle: (i) flow acceleration, t/T=0.035; (ii) peak systole, t/T=0.16; (iii) flow deceleration, t/T=0.35; (iv) peak retrograde flow, t/T=0.55; (v) early diastole, t/T=0.77; (vi) late diastole, t/T=0.87.

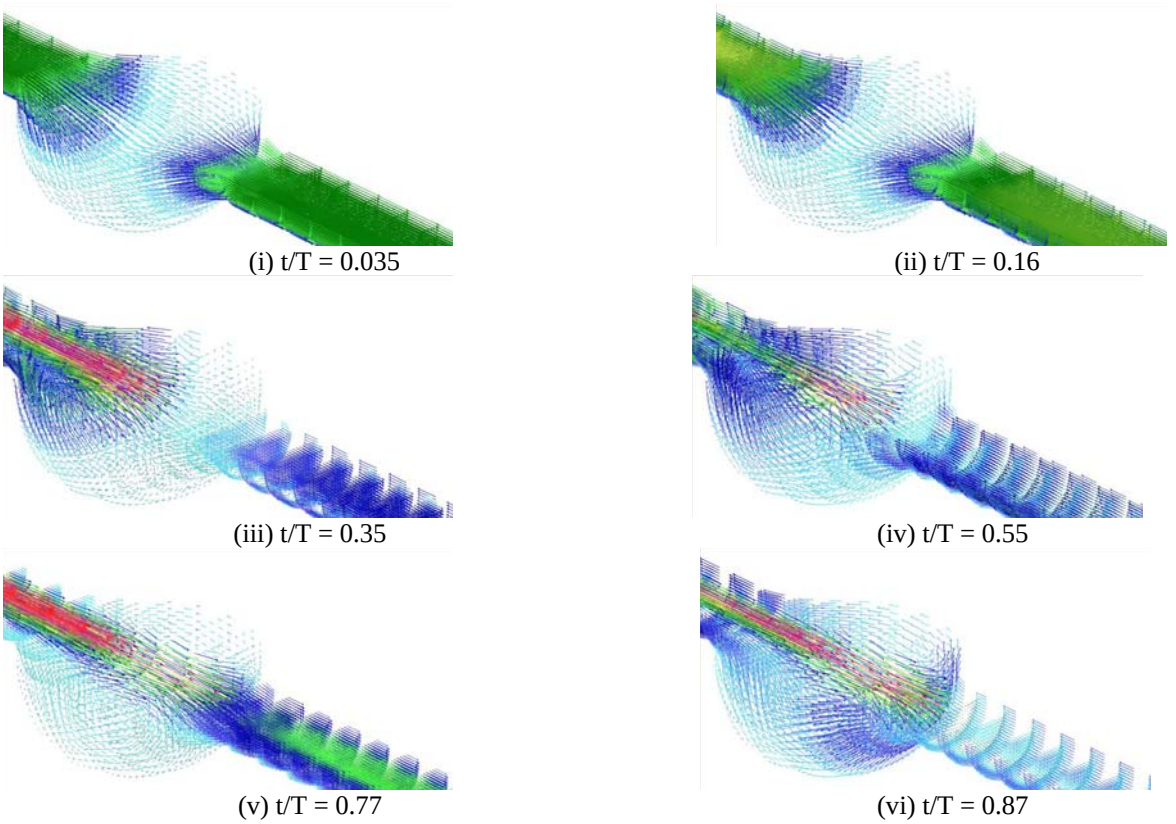

Figure 8. 3D Velocity flow field vectors at six phases of the pulsatile flow cycle: (i) flow acceleration, t/T=0.035; (ii) peak systole, t/T=0.16; (iii) flow deceleration, t/T=0.35; (iv) peak retrograde flow, t/T=0.55; (v) early diastole, t/T=0.77; (vi) late diastole, t/T=0.87.

until the next systolic acceleration began.

As an illustrative example, Figure 9 shows the evolution of secondary velocity distributions at each cross-sectional area of the model starting from the proximal zone of the model bulge right up to the distal zone at peak retrograde

The flow-induced wall shear stress (WSS) distribution throughout the model corresponding to the six different pulsatile phases is shown in Figure 10. The effective mean wall shear stress (WSS_{mean}) at six different pulsatile flow stages and the time-averaged WSS_{mean} throughout the model for a full pulsatile cycle are calculated using Equation (23), where $\boldsymbol{t}_s$ is the surface traction vector, and are illustrated in Figures 11 (i) and 11 (ii), respectively:-

$$\tau_{mean} = \left| \frac{1}{T} \int_0^T t_s dt \right| \qquad (23)$$

In Fig. 11, -0.28<x/D<0.28 refers to the area along the model bulge, whereas x/D<-0.28 and x/D>0.28 refer to the areas along the model entrance and exit, respectively. During flow acceleration to peak systole, the wall shear stress along the model entrance was highest. This is because during this phase, all the flow was forward and consequently the flow exerted force on the wall in the forward direction, i.e. from proximal to distal. The maximum values of wall shear stress were achieved during flow acceleration to peak systole.

At peak systole, a significantly high concentration of wall shear stress was evident at the distal zone of the model bulge. However, the wall shear stress in this region had a far lower magnitude than the wall shear stress observed during flow acceleration to peak systole. During flow deceleration from peak systole into the retrograde flow region, as the recirculation vortex developed in the model bulge, the magnitude of the wall shear stress fell almost to zero. Although there were high concentrations of wall shear stresses at the distal and proximal zones of the model bulge during early diastole and late diastole, respectively, their magnitudes were very low. Throughout the flow cycle, there were no peak wall shear stresses inside the model bulge, so most peak stresses were evident either at the proximal or the distal zones of the bulge.

The flow-induced pressure for the model at six different pulsatile flow phases is shown in Figure 12. One key feature is that the magnitudes of flow-induced pressure tended to decrease from the proximal zone to the distal zone. The pressure along the entrance of the model bulge was always higher than the pressure along the bulge. This trend was almost consistent throughout the flow cycle, regardless of the net flow direction. It appears that the presence or absence of recirculation vortices did not influence these pressure trends.

CONCLUSION

A complete set of three-dimensional finite element equations was derived using the mixed velocity-pressure (v-p) finite element method by implementing the Galerkin method and the implicit incremental-iterative procedure for solving the nonlinear Navier Stokes

equations. The set of equations represents blood as a viscous incompressible fluid and can be applied to solve pulsatile flow problems in AAAs. The computational technique of hemodynamic condition analysis in a typical fusiform AAA could help biomedical engineers and software programmers develop vascular-surgical simulation software. This could help physicians to diagnose and design patient-specific treatment plans that would improve patient care. Efforts are being made to develop surgical software simulation packages that are easy to use and easy for vascular surgeons to interpret in terms of the clinical significance of the simulated results. Clinical application of this numerical modeling and the development of predictive methods will occupy biomedical engineers and scientists for many years to come.

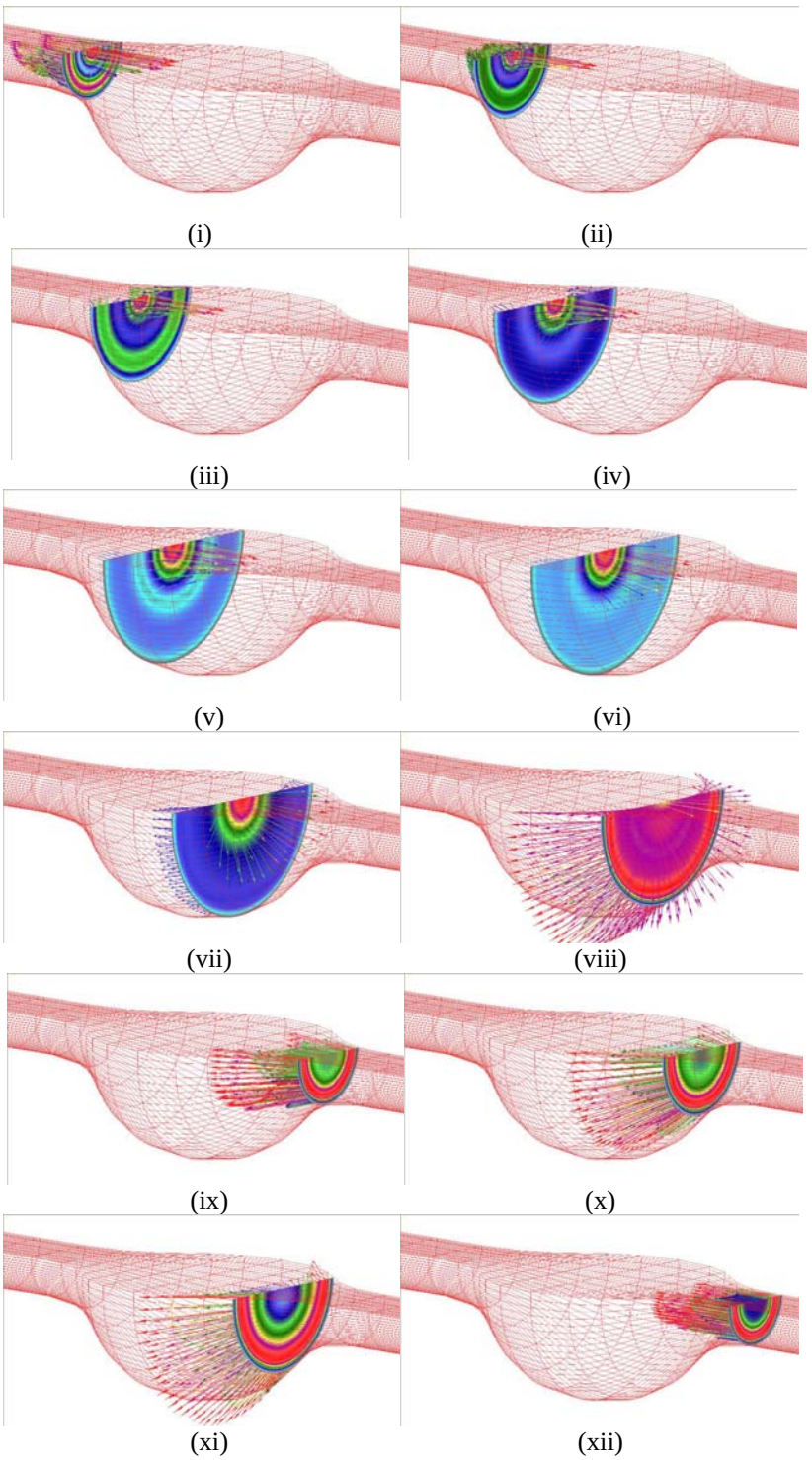

Figure 9. Secondary velocity distributions at each cross-sectional area of the model starting from the proximal zone to the distal zone of the model bulge during peak retrograde flow phase.

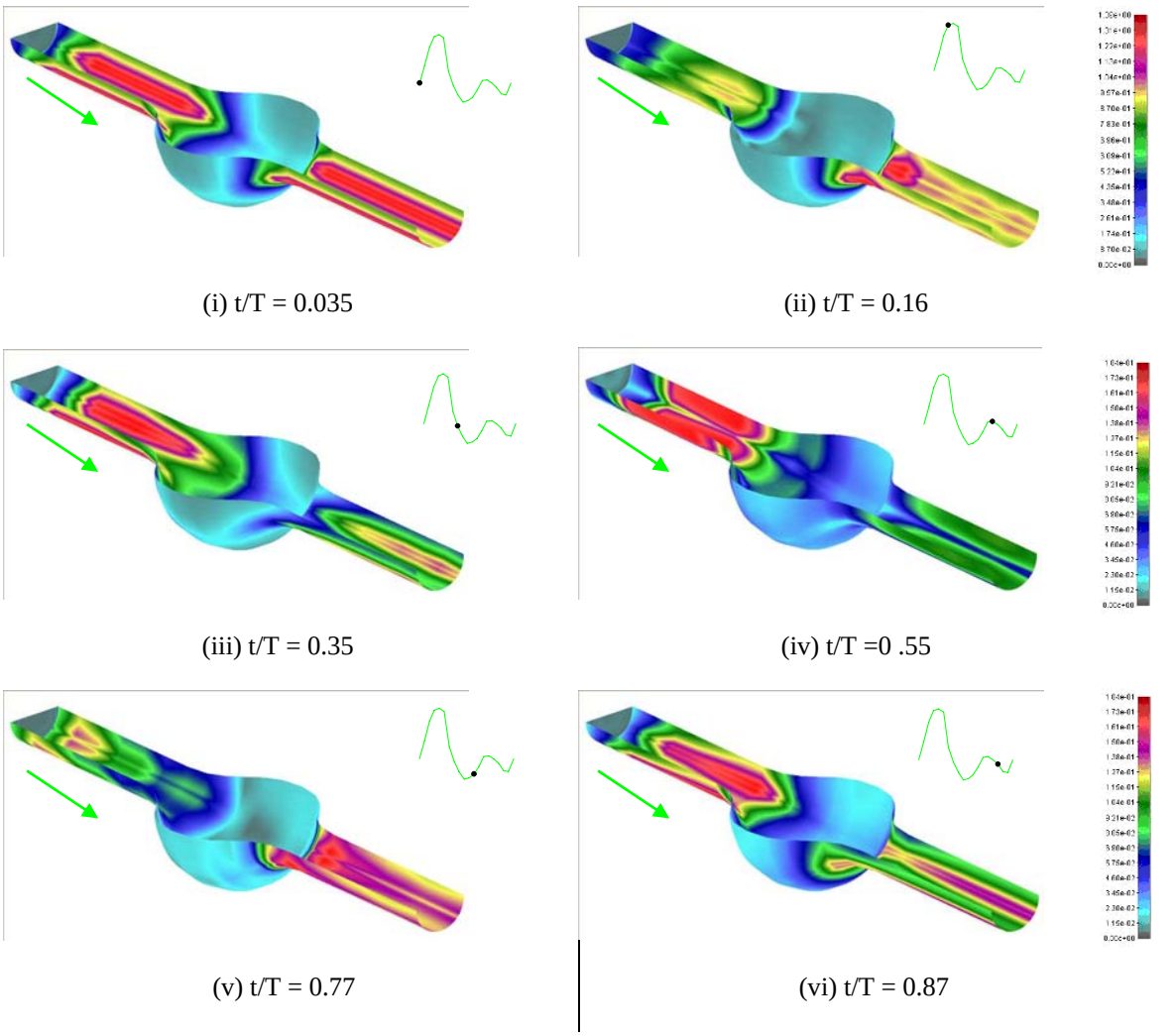

Fig. 10. Flow-induced wall shear stress (WSS) distributions at six phases of the pulsatile flow cycle: (i) flow acceleration, t/T=0.035; (ii) peak systole, t/T=0.16; (iii) flow deceleration, t/T=0.35; (iv) peak retrograde flow, t/T=0.55; (v) early diastole, t/T=0.77; (vi) late diastole, t/T=0.87.

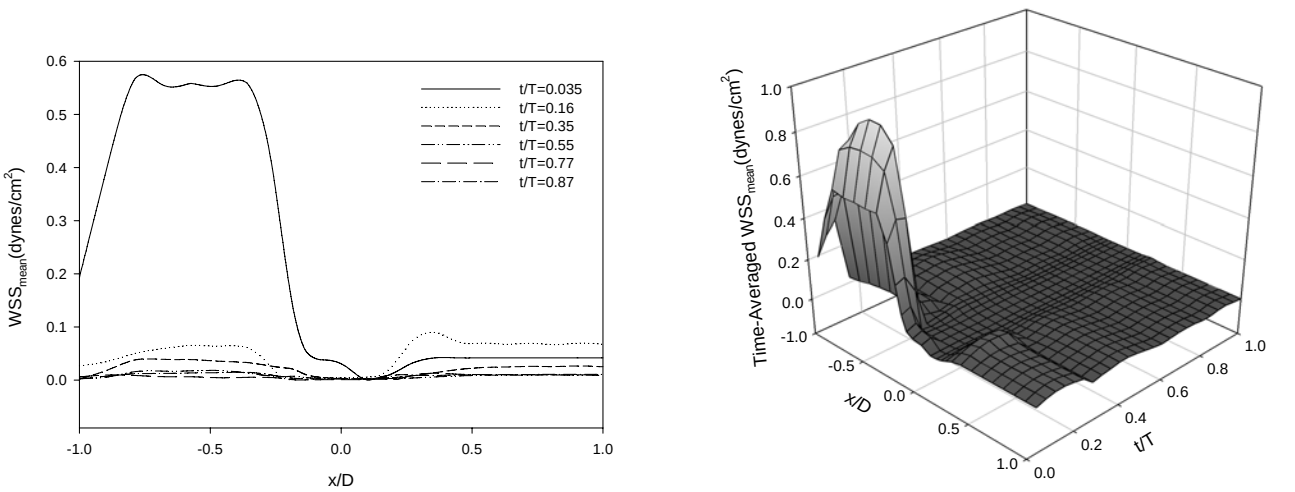

(i) (ii)

Fig. 11. (i) Effective mean wall shear stress (WSS_{mean}) across the model at six different stages of the pulsatile flow cycle; and (ii) time-averaged mean wall shear stress for the entire pulsatile cycle.

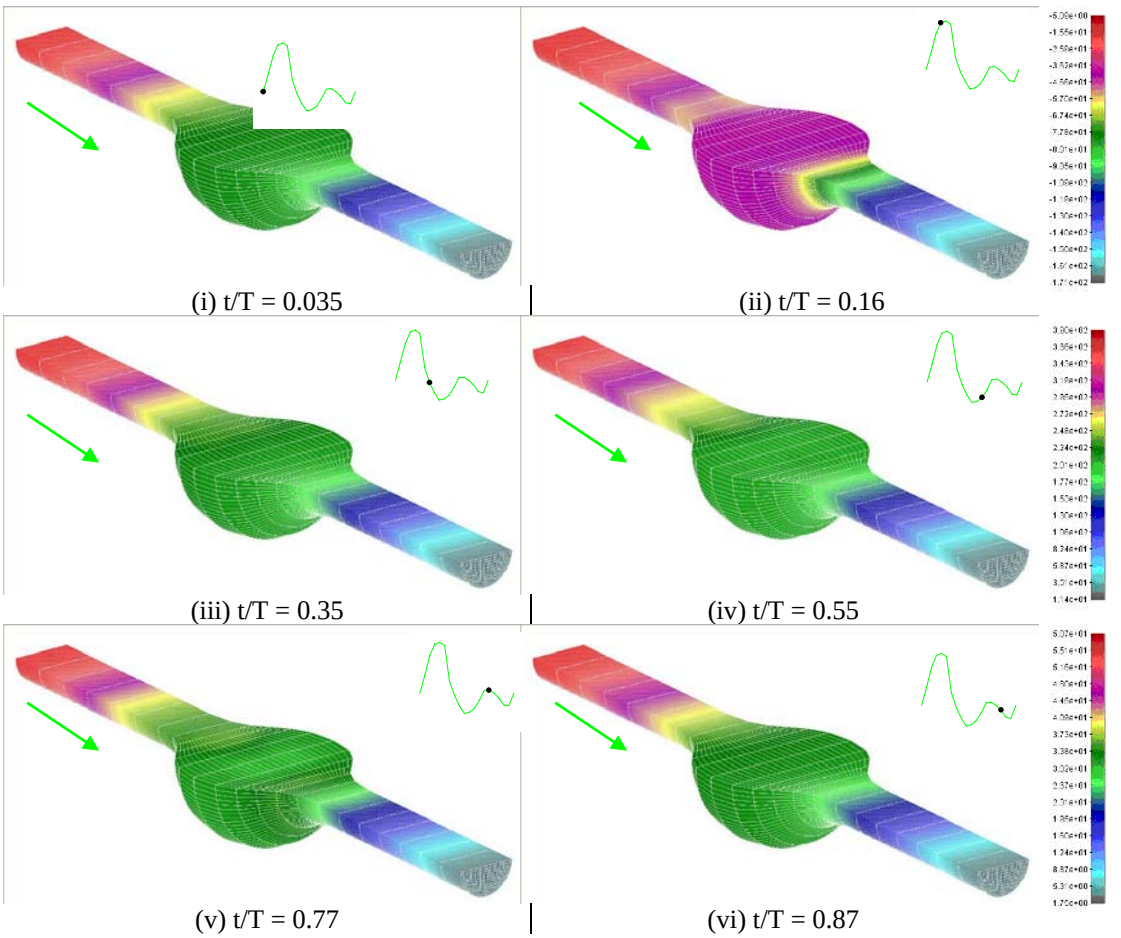

Fig. 12. Flow-induced pressure distributions at six phases of the pulsatile flow cycle: (i) flow acceleration, t/T=0.035; (ii) peak systole, t/T=0.16; (iii) flow deceleration, t/T=0.35; (iv) peak retrograde flow, t/T=0.55; (v) early diastole, t/T=0.77; (vi) late diastole, t/T=0.87.

REFERENCES

1. Cotran RS, Kumar V, Robbins SL, *Robbins Pathologic Basis of Decease*, Saunders, London, 1994.
2. Newman AB, Arnold AM, Burke GL, O'Leary DH, Manolio TA, *Cardiovascular disease and mortality in older adults with small abdominal aortic aneurysms detected by ultrasonography: the cardiovascular health study*, Annals of Internal Medicine 134: pp. 182-190, 2001.
3. Clement Kleinstreuer, Zhonghua Li, *Analysis and computer program for rupture-risk prediction of abdominal aortic aneurysm*, BioMedical Engineering OnLine 5:19, 2006.
4. Myers K, Devine T, Barras C, Self G, *Endoluminal Versus Open Repair for Abdominal Aortic Aneurysms*, http://www.fac.org.ar/scvc/llave/intervine/myers/myersi.htm, 2001.
5. Limet R, Sakalihassan N, Albert A, *Determination of the expansion rate and incidence of rupture of abdominal aortic aneurysms*, Journal of Vascular Surgery 14: 540-548, 1991.
6. Fillinger MF, Raghavan ML, Marra P, Cronenwett L, Kennedy E, *In vivo analysis of mechanical wall stress and abdominal aortic aneurysm rupture risk*, Journal of Vascular Surgery 36: 589-596, 2002.
7. Fillinger MF, Marra PS, Raghavan ML, Kennedy EF, *Prediction of rupture in abdominal aortic aneurysm during observation: wall stress vs diameter*, Journal of Vascular Surgery 37: 724-732, 2003.
8. Peattie RA, Riehle TJ, Bluth EI, *Pulsatile flow in fusiform models of abdominal aortic aneurysms: flow fields, velocity patterns and flow-induced wall stresses.* Journal of Biomechanical Engineering 126: 438-446, 2004.
9. Vorp DA, *Biomechanics of abdominal aortic aneurysm*, Journal of Biomechanics 40: 1887-1902, 2007.
10. Malek AM, Alper SL, Izumo S, *Hemodynamic shear stress and its role in atherosclerosis*, Journal of the American Medical Association, 282: 2035-2042, 1999.
11. Egelhoff CJ, Budwig RS, Elger DF, Khraishi TA, Johansen KH, *Model studies of the flow in abdominal aortic aneurysms during resting and exercise conditions*, Journal of Biomechanics 32: 1319-1329, 1999.
12. Taylor CA, Hughes TJR, Zarins CK, *Finite element modeling of three-dimensional pulsatile flow in the abdominal aorta: Relevance to atherosclerosis*, Annals of Biomedical Engineering 26: 975-987, 1998.
13. Geneves C, Wilquem F, Treyve F, Cloutier G, Soulez G, Saidane K, *Study on non stationary mode flow of an abdominal aortic aneurysm*, Journal of Applied Biomaterials & Biomechanics 3 (3): 176-183, 2005.
14. Filipovic N, Kojic M, *Computer simulation of blood flow with mass transport through the carotid artery bifurcation*, Journal of Theoretical & Applied Mechanics 31 (1): 1-33, 2004.
15. Barth T, Bochev P, Gunzburger M, Shadid J, *A taxonomy of consistently stabilized finite element methods for the Stokes problem*, SIAM Journal of Scientific Computing 25: 1585-1607, 2004.
16. Becker R, Braack M, *A finite element pressure gradient stabilization for the Stokes equations based on a local projection*, Calcolo 38: 173-199, 2001.

17. Boachev P, Gunzburger M, *An absolute stable pressure-Poisson stabilized method for the Stokes equations*, SIAM Journal of Numerical Analysis 42: 1189-1207, 2005.
18. Hughes T, Franca L, *A new finite element formulation for computational fluid dynamics: VII. The Stokes problems with various well-posed boundary condition: symmetric formulations that converge for all velocity pressure spaces*, Computer Methods in Applied Mechanics and Engineering 65: 85-96, 1987.
19. Behr MA, Franca PL, Tezduyar TE, *Stabilized finite element method for the velocity-pressure-stress formulation for incompressible flows*, Computer Methods in Applied Mechanics and Engineering 104: 31-4, 1993.
20. Filipovic N, *Numerical analysis of coupled problems: Fluid flow through porous deformable medium with implementation in biomechanics and geomechanics*, Ph. D. Thesis, University of Kragujevac, Serbia-Yugoslavia, 1996.
21. Shipkowitz T, Rodgers VGJ, Frazin LJ, Chandran KB, *Numerical study on the effect of steady axial flow development in the human aorta on local shear stresses in abdominal aortic branches*, J. Biomech, 31, pp. 995-1007, 1998.
22. Shipkowitz T, Rodgers VGJ, Frazin LJ, Chandran KB, *Numerical study on the effect of secondary flow in the human aorta on local shear stresses in abdominal aortic branches*, J. Biomech, 33, pp. 717-728, 2000.
23. Taylor CA, Hughes TJR, Zarins CK, *Effect of exercise on hemodynamic conditions in the abdominal aorta*, J. Vasc. Surg., 29:6, pp. 1077-1089, 1999.
24. Moore Jr JE, Ku DN, *Pulsatile velocity measurements in a model of the human abdominal aorta under simulated exercise and postprandial conditions*, J. Biomech. Eng., 116, pp. 107-111, 1994
25. Quarteroni A, Tuveri M, Veneziani A, *Computational vascular fluid dynamics : problems, models and methods*, Comp. Visual Sci., 2, pp. 163-197, 2000.
26. Womersley JR, *Method for the calculation of velocity, rate of flow and viscous drag in arteries when the pressure gradient is known*, J. Physiol., 127, pp. 553-563, 1955.
27. Badreddin G, Vijayajothi P, Kahar O, Mohamed Rafiq AK, Kanesan M, *Graphical user interface (GUI) in MatLab for solving the pulsatile flow in blood vessel*, CFDletters, 1:1, pp. 50-58, 2009.
28. Gresho PM, Lee RL, Sani RL, *On the time dependent solution of the incompressible Navier Stokes equations in two and three dimension*, Finite Element in Fluids, **4**: Chapter 2, Gallagher et al, John Wiley & Sons, Chichester, 1982.
29. D. Kwak, JLC Chang, SE Rogers, M Rosenfeld, *Potential applications of computational fluid dynamics to biofluid analysis*, NASA Technical Memorandum, 1988.